Author version: J. Oceanogr.: 64(6); 2008; 831-845

Estimating boundary currents from satellite altimetry: A case study for the east coast of India

F. Durand[1,2], D. Shankar[2], F. Birol[3], S.S.C. Shenoi[2]

(1) IRD, LEGOS, UMR5566 CNRS-CNES-IRD-UPS, 14 Avenue Edouard Belin, 31400 Toulouse, France
(2) Physical Oceanography Division, National Institute of Oceanography, Dona Paula, Goa 403004, India
(3) Center for Topography of Oceans and Hydrosphere, LEGOS, UMR5566 CNRS-CNES-IRD-UPS, 14 Avenue Edouard Belin, 31400 Toulouse, France

Email addresses:
fabien.durand@ird.fr
shankar@nio.org
birol@legos.obs-mip.fr
shenoi@nio.org

Journal of Oceanography, 64, 831-845, 2008.

Corresponding author : Fabien Durand (fabien.durand@ird.fr)
Running title: Boundary currents from altimetry

ABSTRACT

We present a methodology to derive surface geostrophic current from a newly released altimetric sea-level data set. TOPEX/Poseidon data were first completely reprocessed from Geophysical Data Records using new algorithms accommodating marginal seas and coastal conditions. The methodology applied on the reprocessed data essentially consists of a smoothing of the raw along-track coastal altimetric data at the scales at which the geostrophic equilibrium holds. It was reduced to a computational procedure using a set of objective criteria. We applied the method to the East India Coastal Current (EICC) at the western boundary of the Bay of Bengal. This paper first examines the quality of the new data set, which compares well with tide-gauge data; the current we derived is consistent with independent estimates. Our methodology reveals the full spectrum of the along-shore current, ranging from intra-seasonal to inter-annual time scales, from the deep ocean to the shelf-break area where the EICC exists. The algorithm can be applied to any coastal region where an order of the Rossby radius can be defined, and it therefore opens up bright prospects for mapping the variability of other boundary-current systems in the world ocean from altimetry.

1. Introduction

Over the last decade, altimetry has been shown to be a powerful tool to monitor the sea-level variability of the open ocean, leading to tremendous progress in our knowledge of large- to meso-scale ocean dynamics (see Fu and Cazenave (2001) for a review). The use of altimetric products in the coastal domain is, however, still difficult because of two major problems, the interference of radar echo with the surrounding land, and that the standard processing procedure to derive sea level from altimetry has been designed for the open sea and not for marginal seas and coastal regions. Consequently, the error budget of the standard altimetric data sets is often too large to provide a useful observation in the neighbourhood of the coast. The future generation of altimetric missions promises a lot for remote sensing of the coastal sea level: for example, AltiKa (Centre National d'Etudes Spatiales, France / Indian Space Research Organization, India, to be launched in 2009) is a Ka-band altimeter, having a narrower footprint than the standard C-band altimeters such as TOPEX/Poseidon (T/P hereafter) and Jason, and is therefore expected to perform better in the coastal domain.

Nevertheless, some recent studies (Vignudelli et al., 2005; Ollivier, 2006; Bouffard et al., 2008, Volkov et al., 2007) have shown that there is scope for increasing the quality and performance of the existing altimeter missions in the marginal seas. To overcome the processing problems in the derivation of sea level from satellite altimetry in the coastal regions, several groups joined in the Margins Altimetry Project (MAP) to develop a new altimetric-data-processing approach (Roblou and Lyard, 2004; Bouffard, 2007). The MAP algorithms provide corrected Sea Level Anomalies (SLAs) on reference ground tracks, as shall be seen in Section 2. The MAP approach has already been validated in various experimental regions against in situ observations and standard altimetric products. It substantially increases the quantity of valid data in the coastal domain and improves their accuracy (Vignudelli et al., 2005; Bouffard et al., 2008; Bouffard, 2007). Hence, the new MAP along-track data set has considerable potential for coastal oceanographic applications.

In this paper, we use a new sea level data set reprocessed by MAP to demonstrate its capability in bringing out several important features of a large-scale wind-driven boundary current that flows along the western boundary of Bay of Bengal (Figure 1). Called the East India Coastal Current (EICC; Shankar et al., 1996), this current facilitates the exchange of water masses between the Arabian Sea and the Bay of Bengal (e.g. Shetye et al., 1991). Most of the existing knowledge of this boundary current is due to in situ hydrographic observations (e.g. Shetye et al., 1991, 1993, 1996), ship-drift (Mariano et al., 1995) or surface-drifter

(Shenoi et al., 1999) climatologies and modelling studies (e.g. Shankar et al., 1996; Potemra et al., 1991; McCreary et al., 1993, 1996; Vinayachandran et al., 1996), all of which show that the EICC reverses seasonally. The current flows equatorward during boreal autumn and winter and poleward during spring and summer. Nevertheless, though the seasonal cycle of the EICC is reasonably well documented, we know nothing of the variability at intra-seasonal and inter-annual time scales (Shankar et al., 2002).

Thus, in spite of all the knowledge gained from both in situ observations and models, the dearth of continuous observational records of the EICC precludes a description of its full spectrum of variability and of theoretical analyses to decipher the dynamics at time scales other than the seasonal (Schott and McCreary, 2001). The existing gridded T/P data are incapable of capturing the variability of this boundary current at the shelf break owing to the averaging inherent in the gridding procedure: the high spatial resolution along the track is compromised by the low resolution between tracks, making it impossible to capture the offshore structure associated with a boundary current like the EICC. The newly processed along-track data, which yield a far superior cross-shore resolution of the along-shore current (as shall be seen in section 2) overcome these difficulties and present a remarkable opportunity to document the variability of the EICC. Hence, we considered along-track SLA data (i.e., direct observations that are not smoothed by a gridding process) of T/P (track number 116; Figure 1) to capture the intra-seasonal and inter-annual variability of EICC. Apart from its intrinsic climatic interest, the EICC is also particularly well suited to assess the advantages of the new altimetric data set. That sea-level variability is known to be vigorous there (Shetye et al., 1996) makes this track a good test case. T/P track 116 passes very close to Visakhapatnam tide gauge. Hence, it is possible to assess the validity of the newly processed along-track SLA data with long, continuous, high-quality time series of sea level measured by the tide gauge. Also, the shelf break is close to the shore in this region, as shown by the position of the 200 m isobath in Figure 1. As the EICC is expected to be a deep-ocean feature trapped against the shelf break (e.g., Shetye et al., 1996), the narrow shelf limits the potential influence of irrelevant shelf circulation features on the in situ tide gauge signal. This is important because the altimetric signal does not exist on the shelf off Visakhapatnam (Figure 1). Moreover, the T/P track 155 crosses the track 116 at a distance 74 km offshore (that is basically in the area where the EICC exists). This crossover provides an additional opportunity to check the internal consistency of the satellite data set for validation.

In this paper, we demonstrate the ability of the MAP reprocessed sea level data to capture the important features of a large-scale wind driven boundary current, and present a methodology for deriving the along-shore geostrophic current from the along-track data. Section 2 presents the reprocessed altimetric data set and its validation. Section 3 presents the methodology we have used to derive the geostrophic coastal current. The geostrophic current is validated in section 4. Section 5 provides a brief description of the spatio-temporal features of the current revealed by the reprocessed T/P along-track data. Section 6 concludes the paper.

2. Data and processing

a. Data

i. MAP: a new altimetric dataset

The experimental MAP altimetric data processing was originally developed and validated on T/P data in the northwestern Mediterranean Sea after it was shown that an important number of measurements systematically flagged by standard processing were valid and should be recovered (Vignudelli et al., 2000). The resulting new processing strategy was shown to improve both the quantity and quality of altimetric sea surface measurements in the area of the Liguro-Provençal current (Vignudelli et al., 2005). The reader is referred to the Appendix for more details of the MAP processing.

The present study essentially builds on the MAP developments. We reprocessed all the T/P data from cycle 5 (November 1992) to cycle 364 (August 2002) near Visakhapatnam on the east coast of India. Unlike in Vignudelli (2005), we could not take advantage of regional modelling of the high-frequency de-aliasing because, to the best of our knowledge, no regional model is available over the area of interest. Apart from this one difference, we stuck to the same approach. For the particular case of track 116 (see location on Figure 1) that is used in the present study, only the data for cycles 5 (November 1992) to 320 (May 2001) were available. For track 155 (that is used marginally in the present study), the data were available throughout the November 1992 to August 2002 period.

ii. Internal consistency of MAP dataset

The first stage of validation was to assess the internal consistency of our data set by comparing the two tracks (116 and 155) at their crossover point. We do not expect an exact agreement between the two tracks because the random error level of the SLA retrieval is not negligible (of order 5 cm), and because of the time lag between the two passes (track 155 is sampled 1.5 days after track 116). This diagnostic also cannot detect any systematic error in the data set; a systematic error would affect identically the two tracks (typically a poor environmental correction because we could not use regional modeling). Still, this comparison is a reasonable estimate of the "noise" of the altimetric measurements, and hence gives a lower bound of the accuracy of the data. In our case, the root-mean square difference (RMSD) between the two tracks was 6.96 cm, and the correlation between them was 0.82: the two SLA time series shared 67% of their variance, which is comparable to the correlations obtained for standard along-track T/P data for crossover points situated in the open ocean (Bouffard, 2007). Hence, we can use the data set to monitor the large enough (typically of order 10 cm and above) SLAs along the Indian east coast.

b. Comparison of MAP data with standard along-track altimetric products

i. 10-day SLA

We assessed the quality of our new MAP data set as compared to the standard AVISO (1996; hereafter referred to as AVISO) along-track SLAs (available at www.aviso.oceanobs.com/html/donnees/produits/hauteurs/global/sla_uk.html#upd; see www.aviso.oceanobs.com/html/presentation/aviso_uk.html for a general description of the AVISO project) for tracks 116 and 155 (see location in Figure 1). For track 155 (Figure 2 a-c), the standard deviation of SLA in the deep ocean captured by the MAP data set was slightly higher than that of AVISO throughout the track. This difference can be explained by the smoothing applied by AVISO along the track to the data: the smoothing filters out features smaller than 50 km. More striking is the higher variability of the MAP data set as compared to AVISO in the shelf area. The variability of the AVISO along-track data set fell drastically in the area of the shelf break, between 40 km and 45 km off the Indian coast, whereas the MAP data set exhibited maximal variability there. In this area, the standard AVISO processing chain retrieved only 200 valid data points compared to that in the deep ocean (typically 310) (Figure 2b). The reason for this decrease is that the standard criteria used by AVISO processing chain are irrelevant on the shelf to the special physics of the signal measured there, and a significant fraction of the data is lost. On the contrary, the MAP processing allows a better exploitation of the altimeter closer to the coast, as seen from the number of valid data points remaining above 300 all along the track (Figure 2b). The MAP processing increased significantly the quantity of valid data owing to the use of the Bézier polynomial technique, which permits reconstruction of erroneous corrections from valid neighbouring ones and the recovery of data lost by the standard processing (see Appendix). It resulted in a smoother profile of standard deviation (Figure 2a). Moreover, the shoreward increase in the level of variability of SLA in the shelf-break area, captured by MAP, but completely missed by AVISO, is consistent with the linear theory that is thought to govern a prominent part of the

dynamics of the area (e.g., Shankar et al., 1996). As for track 116 (Figure 2 d-f), we can draw similar conclusions: the MAP processing allowed retrieval of a higher level of SLA variability than AVISO; unlike AVISO, it also exhibited a shoreward increase of SLA variability (Figure 2d). For this track, however, MAP does not allow monitoring of the area near the coast: there are no MAP data available within 45 km of the coast, which is the area where the quantity of AVISO data also collapses (Figure 2e).

ii. Monthly SLA

Downgrading the temporal sampling of the altimetric data sets allows a direct validation against the monthly tide-gauge record available from PSMSL (Permanent Service for Mean Sea Level) (Woodworth and Player, 2003) for Visakhapatnam. The monthly averaging of the tide-gauge data ensures removal of the tide. As in Shankar (1998), we used the monthly climatology of COADS (Comprehensive Ocean-Atmosphere Data Set; http://icoads.noaa.gov) sea-level pressure to correct the PSMSL data for the inverse barometer effect (Ponte, 1993). Overall, for the MAP altimetric track section closest to the shore (typically between 45–70 km off the coast), the RMSD between MAP SLA and the tide-gauge signal was comparable to the altimetric SLA variability itself (8–10 cm). For the altimetric point located 47 km offshore, which matched best the tide-gauge data, the correlation with the tide-gauge signal was 0.81 for the monthly climatologies of the two time series. It was about the same over 1992–2001, and is comparable to the crossover point correlation (see section 2.a.ii). That our experimental data set shares about 65% of its variance with the in situ data set at seasonal as well as at inter-annual time scales enables further validation. Hence, we focus on the seasonal cycle of SLA because it illustrates clearly the performance of the altimetric data set.

Figure 3a compares the seasonal climatology of both MAP and AVISO altimetric signals at the point situated 47 km offshore with the tide gauge at Visakhapatnam. There was a broad agreement between the seasonal climatology of the MAP altimetric signal and the tide gauge, with negative SLA (implying a poleward EICC) during the first half of the year and positive SLA (implying an equatorward EICC) after the summer monsoon. This was not the case for the AVISO altimetric signal, which showed positive SLA throughout January-June; during July-December, AVISO SLA had the same sign as the tide gauge and MAP records, but it completely missed the high sea-level peak shown by the tide gauge in November. At this stage, we can see that the realism of MAP product was greater than that of the standard AVISO along-track product: AVISO is not usable at this location situated in the boundary domain.

The peak-to-peak variation was 47 cm (from -18 cm in April to +29 cm in November) in the tide-gauge signal, but was 27 cm (from -14 cm in April to +13 cm in November) in the MAP altimetric signal. This mismatch between the tide gauge and MAP signals was mostly restricted to November and exceeded the bounds of inter-annual variability of the two data sets. Over the rest of the seasonal cycle, the agreement between the two records was remarkable both in phase and in amplitude. The discrepancy was due to the presence of a coastal plume of freshwater that flows past Visakhapatnam in November, thereby inducing a rise in sea level close to the coast (Shankar, 1998). This rise in sea level occurring near the coast is captured by the tide gauge at Visakhapatanam but not by the altimetric signal that terminated at the shelf break. Salinity has been shown by other studies also to have an impact on the tide-gauge sea level along the Indian east coast over a range of time scales (Shankar, 1998; Shankar and Shetye, 1999, 2001; Han and Webster, 2002). Hence, the mismatch between tide-gauge and MAP altimetric time series in November is not due to any flaw in the MAP data.

3. Estimation of the surface boundary current

We define here an objective, easy-to-automate method to make it readily usable for oceanographic purposes. Our principle is to rely only on obvious physical assumptions (geostrophic equilibrium holds), on known geophysical parameters (the length of the Rossby radius of deformation (*Ro* hereafter)), and on common sense (the magnitude of the current in the region of interest cannot exceed a certain threshold). Figure 4 presents a flow chart of the method, it being easy to proceed from the above assumptions to a computational procedure or algorithm. Figure 5 illustrates the various steps of the algorithm, by application to the MAP dataset along T/P track number 116 during summer 1994. The first step of the procedure was to remove the outliers in the raw MAP SLAs by imposing a bound on the cross-track geostrophic current estimated using two neighbouring points:

$$u = g/f\, \partial\eta/\partial x, \qquad (1)$$

where u is the cross-track surface current (almost equal to the along-shore current in the particular case of track number 116, as seen in Figure 1), g is the acceleration due to gravity, f is the Coriolis parameter, η is the SLA, and x is the co-ordinate along the altimetric track. We assumed that the magnitude of the boundary current cannot exceed 2 m s^{-1} in our area of interest (Schott et al., 1994). Equation (1) then yielded an equivalent threshold for the acceptable sea-level difference between two neighbouring altimetric points; the sea-level threshold was 4 cm because the distance between neighbouring points was 6 km for the 1 Hz sampling. Application of this criterion allowed detection and elimination of the outliers (Figure 5b). The resulting SLA profiles were significantly smoother, but still too noisy to be used for current retrieval without smoothing.

The second step of the procedure was to eliminate scales smaller than that at which geostrophic adjustment takes place in the ocean. It is well known that only at spatial scales greater than one *Ro* does the current field adjust to the mass field in a stratified rotating fluid; at scales smaller than *Ro*, the mass field adjusts to the current field. *Ro* is approximately 60 km in our area of interest (Chelton et al., 1998), implying that Equation (1) can be applied only at scales greater than 60 km. Hence, we filtered out the undesirable sub-mesoscale features by a simple polynomial fit. Before doing this fit, however, the same length scale, *Ro*, was used to eliminate gaps in the along-track data. Since it is not possible to fit a polynomial in the presence of a data gap longer than one *Ro*, the presence of such long gaps implied breaks in the SLA curve, the polynomial being fitted separately to each continuous part of the SLA curve. Gaps smaller than one *Ro* were retained, it being possible to fit a polynomial through these gaps. Given the length L of the coastal altimetric track (250 km for the case of track 116), it is straightforward to define the largest possible degree D_{max} of the polynomial to be fitted to the along-track SLA profile:

$$D_{max} = L/Ro + 1. \qquad (2)$$

Note that Equation (2) applies to each part of the SLA curve, these parts being separated by gaps longer than one *Ro*. Indeed, Equation (2) implies that the geostrophic current derived from the fitted SLA could be of maximal degree L/Ro (L being either the length of the track, i. e., 250 km, or the length of a part, the minimum length being one *Ro*), and therefore would have at most L/Ro zero-crossings over the altimetric track length. In other words, there would be at most L/Ro current reversals (and thus at most L/Ro oceanic circulation features) over the track length. For every altimetric cycle, we fitted (in the classical, linear least-squares sense) successively zeroth-order, first-order, …, D_{max} -order polynomials to a given altimetric profile, and retained the lowest-order polynomial fit that satisfied a pre-defined standard deviation threshold (2.5 cm) as compared to the original profile. Figure 5c illustrates the smoothing procedure for the particular example chosen. In this case, the maximal degree D_{max} was five. For most of the altimetric cycles during 1992–2001, the fitted polynomial was of degree 2 or 3 (Table 1).

Note that both these steps, i.e., removal of outliers and fitting of a polynomial, perform the same function: they filter out the variability at scales less than one *Ro*. It is possible to fit the polynomial to the raw SLA profile, but removing the outliers explicitly ensures that the

polynomial is not biased by noise beyond an acceptable threshold. In other words, we have split the polynomial-fitting step of the procedure into two explicit steps, the first eliminating the noise beyond a specified threshold and the second fitting a smooth curve to the (remaining) data (points).

The third (and final) step of the procedure was to estimate the geostrophic surface current, this being a trivial task since the SLA was given by a polynomial function. The procedure yielded a smooth current profile along the track (Figure 5d).

4. Validation of the current

a. Comparison of MAP-derived current with the current derived from standard gridded altimetric product

In this section, we compare the MAP data set with the standard gridded AVISO product (SSALTO/DUACS User Handbook, 2006) normally used in large-scale oceanography (see, for example, Shankar et al., 2002). Along T/P track 116, broadly orthogonal to the western boundary of the Bay of Bengal (see location in Figure 1), we extracted the AVISO gridded field (1/3°, 7 days). For each along-track altimetric point, we picked the nearest AVISO grid point to make the comparison. Then, for the two data sets, gridded AVISO and along-track MAP, for each pair of neighbouring altimetric points, we computed the cross-track geostrophic surface current during 1992–2001. The MAP-derived current was computed by applying routinely the algorithm described in the previous section. Finally, we computed the Lomb periodogram of the estimated current. This technique was needed because the along-track altimetric products have data gaps, which implies a gappy time series that is not amenable to standard Fourier spectral decompostion. We used the algorithm described by Press et al. (1992) to compute the periodograms, but with a modification. Since we want to compare the amplitude of the periodogram between various points along the altimetric track, we did not normalize the periodogram by the overall variance of the time series. Hence, the obtained power was dimensional. Figure 6 presents the results for the annual period (365 days). Note that one cannot compare the magnitudes of the two curves because the temporal sampling is different for the gridded AVISO (7 days) and along-track MAP (10 days) products. Nevertheless, it is important to note the fundamental difference in the patterns exhibited. Though there was general broad agreement between the gridded product and our along-track experimental data set in the deep ocean, the two data sets exhibited marked differences in the level of variability in the shelf break area. In the case of the gridded product (Figure 6b), the signal energy increased from the deep ocean (150 km offshore) towards the coast, up to a maximum that was reached ~ 90 km offshore; shoreward of this location, the energy collapsed dramatically. On the contrary, for the along-track MAP product (Figure 6a), the energy of the signal increased continuously from the deep ocean to 50 km offshore. Just like for SLA, this coastal trapping of the along-shore current variability at annual period is well explained by linear theory (e.g., Shankar et al., 1996) and clearly seen in numerical simulations (e.g. McCreary et al., 1993, 1996). According to the theory, the trapping is expected to occur over one *Ro* off the shelf break, which is ~ 60 km for track 116 (Chelton et al., 1998). The fundamental difference in the behavior of the two data sets in the vicinity of the shelf break is robust because of the high statistical significance of both periodograms. This result was corroborated by a computation of long-term standard deviation of the geostrophic cross-track current for the two data sets. While they were in broad agreement off the shelf break, with typical values of 0.3 m s^{-1}, they behaved very differently in the vicinity of the shelf break (Figure 6c): the gridded product showed a peak variance hardly reaching 0.4 m s^{-1} at 90 km offshore, whereas the MAP along-track product attained a variance of 0.65 m s^{-1} at 50 km offshore. As far as the large-scale boundary current is concerned, this showed that the smoothing of the SLAs inevitable in the gridding procedure

completely damps the signal over the region of dynamic interest, which is the first *Ro* off the shelf break.

b. Comparison of MAP-derived current with the current derived from standard along-track altimetric product

The current thus derived was then compared with current derived from standard AVISO along-track SLAs (presented in section 2b). This was done through validation against the available information from historical ship drifts. Ideally, direct, in situ measurements of surface currents were necessary for such validation, but such measurements are not available in this region. Hence, we validated our current estimates against historical ship-drift climatologies (1°×1°×1 month) compiled by Mariano et al. (1995) and NOAA (National Oceanic and Atmospheric Administration). For consistency, the spatial resolution of our cross-track altimetric current estimates was downgraded to 1° (i. e., 110 km) by averaging. For comparison, we considered the point that is closest to the shore (at 17°N, 84°E) in the low-resolution grids. Figure 3b presents the seasonal climatology of the various products after projection in the cross-track direction. We can compare the altimetry-derived current anomalies to the ship-drift data, which represent absolute velocities because the mean component of the EICC is known to be weak in comparison to its seasonal cycle (Schott and McCreary, 2001; Shankar et al., 2002). Also, the ageostrophic (typically Ekman) component of the current, which is included in the ship-drift data, but is not accounted for in our derivation of the current from the altimetric signal, was found to be weak (at most of order 0.1 m s^{-1} during June–August) in our area of interest. We can see a broad agreement of the various ship-drift estimates with both altimetric currents. The EICC flowed poleward during the first half of the year (reaching a speed of 0.5–0.7 m s^{-1}), a reversal occurring sometime during the summer monsoon; the EICC flowed equatorward during the post-monsoon season (with the peak speed ranging from 0.4–0.7 m s^{-1}), reversing again at the end of the year. The AVISO-derived current is comparable with the other estimates, but it appears excessively smooth. Its peak-to-peak variation hardly reaches 0.60 m s^{-1} (from 0.30 m s^{-1} in March to -0.30 m s^{-1} in November), but the peak-to-peak variation exceeds 0.80 m s^{-1} in MAP and 1 m s^{-1} in both the ship-drift products. The current time series basically mirrored the coastal SLA time series of Figure 3a. During January–June, SLA at the coast was negative, the sea level sloping down toward the coast, and the geostrophic current was poleward; the opposite picture held during the other season. This agreement between coastal sea level and boundary current was also noted by Shankar (1998, 2000). Superimposed on this low-frequency picture was a marked spread between the two ship-drift time series. This intra-seasonal variation is linked with the high level of uncertainty in the ship-drift velocity compilations. Given this uncertainty, we can see that our MAP-based estimate is in reasonable agreement with all the ship drifts, whether we take into account the Ekman flow or not.

At this stage, we have seen that MAP SLAs compare well with tide-gauge data, and are significantly better than the standard along-track product. The MAP-derived current successfully captures the coastal trapping of EICC variability, unlike the current derived from standard gridded SLA product. We have also seen that MAP-derived current compares reasonably well with the ship-drift products within their error bound; it also shows a more energetic seasonal climatology than the current derived from the standard along-track product, even though the improvement brought by MAP over the standard product is less dramatic for the current than for the sea level. The combination of all these factors leads us to the conclusion that MAP is the best-suited product for the purpose of this study.

5. Variability of the current

In the rest of the study, we use the MAP-derived current data to describe the variability of the current in space (cross-shore dimension) and time.

a. Spectral analysis

In order to identify the time scales of variability of the EICC, we carried out a spectral analysis. We extended the computation of Lomb periodogram, presented in Figure 6 for the annual period, to all periods (i. e., from 20 days to 10 years). After doing so, we stacked together the periodograms obtained for all the points along the track to construct the matrix plotted in Figure 7a. Three spectral bands were statistically significant at the 99% level (in the sense described by Press et al. (1992)): one at intra-seasonal time scale, one at annual time scale, and one at inter-annual time scale.

i. Intra-seasonal band

The intra-seasonal band showed a sharp peak centered on 156 days (Figure 7a and 7b). Even though intra-seasonal variability existed throughout the altimetric track (not shown), only the central part, situated off the shelf break between 100 km and 185 km from the coast, passed the 99% significance threshold of Press et al. (1992). Also, the absence of significant periodogram values at intra-seasonal time scales other than 156 days does not imply that the current does not show any variability in this range; actually, the intra-seasonal time scales concentrate more energy than the rest of the spectrum, as shall be seen in the next section. The reason for this seeming lack of intra-seasonal energy in the periodogram is that the periodogram can only capture those periodic signals that do not show too many phase changes over the record period. If the intra-seasonal variability does not show any clear phase continuity (which is the case here; see section 5.b), then the periodogram computation is bound to underestimate its importance relative to the annual time scale (tightly locked to the monsoonal cycle) and the inter-annual time scale (which can not contain many phase changes given the limited length of the record). We are not aware of an earlier report of this time scale of variability of the EICC in this area, but Nethery and Shankar (2007) found a similar peak (though at a slightly shorter period, around 120 days) in the spectrum of the shallow current-meter data from south of Sri Lanka (Schott et al., 1994). Though this location is far south of our altimetric track, the two features might be linked because the EICC and the monsoon currents south of Sri Lanka are dynamically linked (Shankar et al., 2002). Still, the processes driving this intra-seasonal variability at the western boundary of the Bay of Bengal are unknown.

ii. Annual band

The annual period was the most powerful of the whole spectrum (Figure 7a and 6a). It spanned the complete altimetric track, from the coastal domain to the deep ocean. It has been simulated successfully by a variety of numerical models (e.g., McCreary et al., 1993, 1996). As shown by Shankar et al. (1996) and McCreary et al. (1996), the annual variability of the EICC is fairly well explained by linear dynamics and is known to be driven by the annual periodicity inherent in the monsoonal forcing. Hence, it is expected to be coastally-trapped (the current is trapped at the shelf break), with a trapping length scale of about one *Ro*. We can see the trapping of the annual energy against the shelf break, suggesting an exponential decay with respect to the offshore distance; the typical *e*-folding scale was of the order of 55 km (Figure 6a). In the linear framework of coastally trapped Kelvin waves (see e.g. Gill, 1982), the *e*-folding scale of the periodogram of the along-shore current should be of one half of *Ro*, viz. 30 km in our area (Chelton et al., 1998). We can see that the other dynamical effects not accounted for by the linear theory tend to spread the coastal trapping of the energy in the offshore direction. About 200 km off the coast, the power of the annual component increased in the offshore direction, suggesting that another regime, dynamically distinct from the coastal waveguide, exists there.

iii. Inter-annual band

At inter-annual periods (Figure 7a and 7c), there were two broad blobs between 3–4.5 years, one clinging to the shelf break between 55 km and 85 km from the coast and the other

at the offshore edge of the track in the deep ocean. The coastal part of the pattern may be related to the known inter-annual variability of sea level reported by Clarke and Liu (1994) and Han and Webster (2002) from the analysis of Visakhapatnam tide-gauge record, but the deep-ocean feature centered about 220 km offshore has not been reported before.

b. Spatio-temporal variability

In this section, we discuss the time evolution of the derived current over the entire record for each of the above three spectral bands. To isolate the various components, we filtered the original time series of the current by applying moving-average filters. We used a high-pass 250-day window to isolate the intra-seasonal frequencies and a low-pass 500-day window to isolate the inter-annual frequencies. The annual frequencies were then the residual of these two filtering operations being applied in succession. For each of the three time scales, we present the time series of the along-shore current, which is defined as the projection of the cross-track current in the along-shore direction; the projection coefficient (i. e., the cosine of the angle between the altimetric track and the shore direction) was 0.95 for track 116. Strictly speaking, we discard the along-shore component of the along-track current in doing so, but this error should be negligible because the altimetric track is almost normal to the coast (Figure 1). We considered three contrasting locations along the altimetric track, one situated in the core of the EICC in the coastal waveguide (called EICC), one situated at the offshore edge of the track in the deep ocean, and one situated in between them in the transition region.

i. Intra-seasonal time scales

Figure 8a presents the time evolution of the intra-seasonal component of the current. Peak-to-peak variations of the EICC reached ±1 m s^{-1} on some occasions. A low-frequency modulation of this intra-seasonal variability was clearly visible, with relatively low variability during certain periods (first half of 1995, 1997, and 2000) and relatively high variability during other periods (1994, 1996, and 1999). The current at the offshore point presented similar features, but was less energetic. The currents at the two locations were often out of phase, particularly during the intense intra-seasonal events of early 1994, late 1994, early 1996, and mid-1999. There were, however, some occasions when this sheared structure disappeared (e.g., mid-1995). The current at the intermediate point in the transition region (where the periodogram of Figure 7 showed a large power) followed the evolution of the EICC point most of the time, though with a lesser amplitude.

The intra-seasonal component of the AVISO along-shore current is also shown for comparison. The two products (MAP and AVISO) presented marked differences for the three points we selected. For example, the EICC point (grey curve) showed a 1m s^{-1} intra-seasonal northward peak in November 2000 in the AVISO product (Figure 8d), but it was hardly 0.5 m s^{-1} in the MAP time series at this time (Figure 8a). Conversely, there was a -1 m s^{-1} (southward) peak in MAP in November 1996, but it was just -0.3 m s^{-1} in AVISO. Note, however, that there is no independent data set against which either data set can be evaluated. Hence, the superiority of the MAP product has to be inferred from the comparisons described earlier in sections 3 and 4.

ii. Annual time scales

Figure 8b presents the annual component of the current. The EICC showed a cyclic evolution, consistent with climatological picture of Figure 4b: for most of the years during mid-1993 to mid-2000, the EICC was poleward during the first half of the year; it reversed sometime around the beginning of July, and flowed southward until the end of the year. The peak-to-peak variation was typically ±0.3 m s^{-1}. One exception was the period between mid-1997 and late 1998: over this period, the seasonal cycle of the EICC virtually disappeared, with the speed hovering around zero. The offshore point showed a similar alternating behaviour, but, consistent with the periodogram in Figure 7, had a smaller amplitude. The most prominent feature was the quasi-systematic shear of the current between the EICC and

the offshore region. Only during the anomalous period from mid-1997 to late 1998 did the two time series not appear out of phase. The reason for this discrepancy is unclear, but it is known that the tropical Indian Ocean exhibited marked basin-scale thermohaline anomalies during this period (e.g., Saji et al., 1999; Han and Webster, 2002). Over the remainder of the time series, the current exhibited a shear between the EICC and the offshore region. The intermediate point appeared as a pivotal location of the seesaw structure, with a weaker amplitude of the current, and values consistently between those at the two extremities.

The AVISO annual component (Figure 8e) compared better with the MAP annual component than did the intra-seasonal component, but there were still differences between the two data sets.

iii. Inter-annual time scales

Figure 8c shows the low-frequency, sub-annual evolution of the current. Consistent with the dominant periodicity of 3–4.5 years identified by spectral analysis (Figure 7), we found two cycles of the oscillation in the EICC, with poleward anomalies from mid-1993 to late 1994 and from mid-1997 to early 1998, and equatorward anomalies during the rest of the time series. The peak-to-peak variation was typically ± 0.2 m s^{-1}, which is not negligible in comparison with the seasonal variation (Figure 8b). The offshore current exhibited a similar behaviour, with peak-to-peak variation of about ± 0.1 m s^{-1}. Just like for the intra-seasonal and annual time scales, the two time series were quasi-systematically out of phase at inter-annual time scales too. The intermediate point showed a weaker variability than that at the two extremities, except during the anomalous period from mid-1997 to mid-1998.

The comparison between the AVISO inter-annual component (Figure 8f) and the MAP inter-annual component was similar to that for the annual component. At low frequencies, the averaging in the AVISO product had less impact on the current, but there still were differences between the two products.

Overall, AVISO-derived current (Figures 8d,e,f) exhibited slightly more variability than MAP-derived current (Figures 8a,b,c) at the EICC point. The excess variability in AVISO, however, exceeds the MAP standard deviation by 3% (at intra-seasonal and inter-annual timescales) and 7% (at annual timescale) only. This stands in contrast with the overall excess variability seen in MAP-derived current climatology as compared to AVISO-derived current climatology (Figure 3b). Hence, this particular feature of AVISO dataset at point 39 cannot be considered as representative of the EICC as a whole.

6. Concluding remarks

We have presented a method to derive the geostrophic surface boundary current from along-track satellite altimetric profiles. This method is objective, in that it relies only on the geophysical parameters such as the length of the Rossby radius of deformation or the maximal acceptable magnitude of the surface current. As such, it can be automated, leading to a computational procedure that is applicable to practically any oceanic region. Based on the recently released MAP coastal altimetric data processing chain, we validated the retrieved T/P SLAs, as well as the currents derived from these SLAs, at one site in the western Bay of Bengal. We proved the quality of the SLA at 10-day frequency and in monthly climatological conditions by comparison with independent data sets. The successful validation of the cross-track geostrophic current we derived was conducted to the extent of the available in situ current data, which are fairly scanty.

We then presented the temporal and spatial variability of the along-shore current, both in the shelf-break area and slightly offshore in the deep ocean. The reprocessed coastal sea levels allowed the retrieval of a wide spectrum of variability in the large-scale coastal currents, from intra-seasonal to inter-annual time scales. It also revealed a peculiar feature of the western Bay of Bengal, with a quasi-systematic reversal of the current between the core of

the EICC and the region situated about 180 km offshore of it. This was a robust feature at all the time scales we could observe. The underlying mechanisms are unknown, and need to be identified; such an analysis is clearly beyond the scope of the present paper and will form the subject of a future study.

Still, this feature was not an artefact of our algorithm. Indeed, the surface geostrophic current derived from AVISO gridded SLAs reveals that a quasi-stationary eddy hugs the east coast of India at this location. It is alternately cyclonic and anticyclonic. The EICC corresponds to the shoreward (north-western) flank of the eddy and the offshore current we identified in section 4 corresponds to the recirculating branch. Figure 9 illustrates this eddy for three representative cases. We draw the reader's attention to the cautious interpretation required of the SLA pattern captured by AVISO product: even though it is known to be trustworthy in the deep ocean far enough from the shelf break (where the eddy centre is located), one can not trust the details of the coastal arm of the recirculations, and in particular the magnitude (as seen in section 4). In late May 1994, our algorithm revealed that the EICC was poleward and the offshore current was equatorward (Figure 5). This is consistent with the anticyclonic circulation seen in the raw (unfiltered) AVISO-derived geostrophic surface current at this time (Figure 9a). To check whether the same conclusion holds at low frequency (annual and inter-annual), we then applied to the AVISO gridded data set the same filtering procedure as we applied to the along-track data set (see section 4.b). In September 1993, the annual EICC we retrieved was equatorward and the annual offshore current was poleward (Figure 8b), matching the structure of the cyclonic recirculation seen in the gridded product (Figure 9b). As for the inter-annual signal, in June 1999, the EICC was equatorward and the offshore current was poleward (Figure 8c). Again, this matches the cyclonic structure seen in the corresponding gridded product (Figure 9c). The three situations we just presented are not particular cases: we could see that throughout 1993-2000, the shear of the along-shore component of the current revealed by our approach was consistent with the pattern seen in the gridded product (to the extent of its accuracy in the boundary area). The typical horizontal scale of the recirculation exceeds two degrees, irrespective of whether it is cyclonic or anticyclonic, and it exists at all the time scales we could observe (not shown). Given that the scale of this feature exceeds *Ro*, it is reassuring to see that our method captures it successfully. All the benefit of our approach lies in the coastal flank of the eddy, where the gridding procedure of AVISO excessively smoothes out the cross-shore slope of sea level, and therefore underestimates the magnitude of the along-shore boundary current (Figure 6c).

Basically, the above method should be tractable anywhere in the world ocean, provided the Rossby radius of deformation can be defined (i. e., everywhere except strictly along the equator). Beyond the Bay-of-Bengal case study presented here, the generic character of our methodology holds promise for a broad range of studies, typically in those numerous regions where the surface boundary circulation is supposed to be of great interest, but is difficult to monitor with in situ measurements. Given the dearth of direct current measurements along the coasts of the north Indian Ocean, this region is one where this method holds considerable promise for advancing our knowledge of the variability of the boundary currents.

The most recent improvements added to the MAP processing, i. e., higher sampling rates as well as multi-satellite (T/P, Jason, Envisat, and Geosat-Follow-On) data algorithms substantially increase the amount of available data. The combination of all these data sets will allow us to monitor sea-level variations in the coastal domain with a very good resolution. In particular, such satellite data, which permit a 0.1 Hz (0.7 km) resolution along the track, should allow our methodology to be usable in high latitudes, where the Rossby radius is much smaller than in the tropics. This opens up the way to new applications for satellite altimetry in marginal seas.

Appendix : the MAP processing of altimetric data

For the present study, T/P data for the period November 1992 (cycle 5) to August 2002 (cycle 364) have been reprocessed from the Geophysical Data Record (GDR) data stream at a rate of one-per-second (spacing of 6 km along the satellite track) distributed by AVISO. The corrections that are applied to the raw altimetric measurements consist of the usual set: dry and wet tropospheric corrections, electro-magnetic bias, ionospheric correction, ocean and loading tidal effects.

Given that altimetric observations close to the coast are degraded in accuracy, the processing starts with the selection of valid ocean data. To do so, a precise land mask and a dedicated editing strategy are used. The latter includes two steps. The first step is to impose editing criteria on T/P measurements and on the corrections. These criteria are more restrictive than the standard ones used by AVISO. Indeed, one of the reasons for the unrealistic large variability often observed in T/P AVISO data near continental shelves is the presence of many outliers in the corrections. To solve this problem, the behaviour of all the corrective terms is analysed along the track. Abrupt changes are assumed to be associated to erroneous data. Outliers are removed by means of a 3σ filter, where σ is the standard deviation of the original along track record. One value of σ is computed per satellite cycle and per corrective parameter, so as to account for the natural temporal variability of the corrections. The threshold of 3σ was optimized after various tests, in order to ensure that the outliers are totally removed. Not only are the outliers eliminated, but also the neighbours that often contain deficient values. Since the editing process leads to the rejection of all altimeter measurements for which at least one correction is identified as erroneous, this strategy rejects much more data than does the standard processing chain of AVISO.

Data analysis indicates that on many occasions, a careful interpolation along the track of corrective parameters to fill the gaps left by the rejected outliers allows recovering valid altimeter observations (Birol et al., 2006). Therefore, in the second step, every corrective parameter was recomputed using Bézier interpolation curves along the track, based on the valid data available in the neighbourhood. This approach allows retrieval of a significant amount of good altimetric measurements that are flagged in the standard AVISO product.

Once the usual corrections were applied, we removed the unresolved high-frequency signals generated by the tidal and atmospheric forcing using, respectively, the FES2004 solution (Letellier et al., 2004) and the global MOG2D barotropic model (Carrère and Lyard, 2003). Indeed, on the shelf, the aliasing of these high frequency signals (typically: tides and storm surges) is known to be a source of large errors in altimetric data. FES2004 and MOG2D models are finite element models with a finer resolution in coastal zones; their use for the de-aliasing of altimeter records is known to significantly reduce the errors of altimeter measurements in the shallow areas (Volkov et al., 2007).

Individual sea surface height (SSH) altimetric measurements are located randomly within a band of about 2km width, centred on the nominal satellite ground track. Hence they need to be projected on fixed positions along the nominal ground track, in order to produce a repeated data sampling from one cycle to the other. To do so, individual SSH measurements have been corrected from along-track and cross-track slopes of the sea surface given by a precise local mean sea surface. At this kilometric scale, the SSH varies essentially under the influence of the geoid height variation. The mean SSH was calculated by inversion of all the SSH measurements along the repeated ground tracks of T/P. This procedure is important since it was found that, in coastal areas, where the topographic gradients are large, the use of such an accurate mean SSH sea surface leads to significant improvement in the quality of the SLAs retrieved (see Vignudelli et al., 2005, their Figure 2b).

Finally, SSH data are converted into SLAs by subtracting the mean sea-surface value computed at the fixed nominal points.

Acknowledgements. This study was funded by IRD, LEGOS, and NIO. Support from these institutions is gratefully acknowledged. DS and SSCS thank MoES and CSIR, India for financial support. We are indebted to the scientists involved in the MAP project for working out the raw SLA processing algorithm. Fruitful discussions with L. Roblou helped in the initial stage of the study. We thank Lionel Gourdeau, Yukio Masumoto and an anonymous reviewer for constructive suggestions. We made extensive use of the SAXO software (http://forge.ipsl.jussieu.fr/saxo) developed by Sébastien Masson for plotting. This is NIO contribution 4382.

Keywords: Altimetry, geostrophy, coastal current, EICC, Bay of Bengal, monsoon.

REFERENCES

AVISO (1996): AVISO user handbook: Merged TOPEX/Poseidon products, Tech. Rep. AVI-NT-02-101-CN, ed. 3.0, 198pp, Toulouse, France.

F. Birol, L. Roblou, F. Lyard, W. Llovel, F. Durand, L. Renault, B. Dewitte, R. Morrow and Y. Ménard (2006): Towards using satellite altimetry for the observation of coastal dynamics. Symposium "15 Years of Progress in Radar Altimetry", Venice, Italy. http://earth.esa.int/workshops/venice06/participants/855/paper_855_birol.pdf.

Bouffard, J., S. Vignudelli, M. Hermann, F. Lyard, P. Marsaleix, Y. Ménard and P. Cipollini (2008): Comparison of Ocean Dynamics with a Regional Circulation Model and Improved Altimetry in the Northwestern Mediterranean Sea. Terr. Atmosph. Ocean. Sci., in press.

Bouffard, J. (2007) : Amélioration de l'altimétrie côtière appliquée à l'étude de la circulation dans la partie nord du bassin occidental méditerranéen. PhD thesis, Toulouse University, Toulouse, France.

Carrère, L., and F. Lyard (2003): Modeling the barotropic response of the global ocean to atmospheric wind and pressure forcing-Comparisons with observations. Geophys. Res. Lett., 30(6), 1275, doi:10.1029/2002GL016473).

Chelton, D. B., R. A. deSzoeke, M. G. Schlax, K. El Naggar and N. Siwertz (1998): Geographical variability of the first baroclinic Rossby radius of deformation. J. Phys. Oceanogr., 28, 433-460.

Clarke, A. J. and X. Liu (1994): Interannual Sea Level in the Northern and Eastern Indian Ocean. J. Phys. Oceanogr., 24, 1224-1235.

Fu, L.-L., and A. Cazenave (2001): Satellite Altimetry and Earth Sciences. A Handbook of Techniques and Applications. Academic Press, 463pp.

Han, W., and P. Webster (2002): Forcing Mechanisms of Sea Level Interannual Variability in the Bay of Bengal. J. Phys. Oceanogr., 32, 216-239.

Gill, A.E. (1982): Atmosphere-Ocean Dynamics. Academic Press.

Letellier, T., F. Lyard and F. Lefebre (2004): The new global tidal solution: FES2004. Jason SWT Meeting Abstracts, St Petersburg, Florida, USA.

McCreary, J. P., P. K. Kundu, and R. L. Molinari (1993): A numerical investigation of the dynamics, thermodynamics and mixed-layer processes in the Indian Ocean. Prog. Oceanogr., 31, 181-244.

McCreary, J. P., W. Han, D. Shankar, and S. R. Shetye (1996): Dynamics of the East India Coastal Current, 2. Numerical solutions. J. Geophys. Res., 101, 13,993-14,010.

Mariano, A.J., E.H. Ryan, B.D. Perkins and S.Smithers (1995): The Mariano Global Surface Velocity Analysis 1.0,USCG Report CG-D-34-95, 55 pp.

Nethery, D., and D. Shankar (2007): Vertical propagation of baroclinic Kelvin waves along the west coast of India. J. Earth Syst. Sci., 116, 331-339.

Ollivier, A, (2006): Nouvelle approche pour l'extraction de paramètres géophysiques à partir des mesures en altimétrie radar. Ph.D. thesis, Grenoble University, Grenoble, France.

Ponte, R. M. (1993): Variability in a homogeneous global ocean forced by barometric pressure. Dyn. Oceans and Atmosph., 18, 209-234.

Potemra, J. T., M. E. Luther and J. J. O'Brien (1991): The seasonal circulation of the upper ocean in the Bay of Bengal. J. Geophys. Res., 96, 12667-12683.

Press, W. H., S. A. Teukolsky, W. T. Vetterling and B. P. Flannery (1992): Numerical Recipes in Fortran 77, The Art of Scientific Computing. Cambridge University Press, 935pp.

Roblou, L., and F. Lyard (2004): Retraitement des données altimétriques satellitaires pour des applications côtières en Mer Méditerranée. Tech. Rep. POC-TR-09—04, Pôle d'océanographie côtière, Toulouse, France, 15pp.

Saji, N. H., B. N. Goswami, P. N. Vinayachandran and T. Yamagata (1999): A dipole mode in the tropical Indian Ocean. Nature, 401, 360-363.

Schott, F., J. Reppin, J. Fischer, and D. Quadfasel (1994): Currents and transports of the Monsoon Current south of Sri Lanka. J. Geophys. Res., 99(C12), 25,127–25,142.

Schott, F., and J. P. McCreary (2001): The monsoon circulation in the Indian Ocean, Progr. Oceanogr., 51, 1-123.

Shankar, D., J. P. McCreary, W. Han and S. R. Shetye (1996): On the dynamics of the East India Coastal Current, part 1, Analytic solutions forced by interior Ekman pumping and local alongshore winds. J. Geophys. Res., 101, 13975-13991.

Shankar, D. (1998): Low-frequency variability of sea level along the coast of India. PhD thesis, Goa University, Goa, India, 207pp. (http://hdl.handle.net/2264/24).

Shankar, D. (2000): Seasonal cycle of sea level and currents along the coast of India. Curr. Sci., 78, 279-288.

Shankar, D., and S. R. Shetye (1999): Are interdecadal sea level changes along the Indian coast influenced by variability of monsoon rainfall? J. Geophys. Res., 104, 26031–26042.

Shankar, D., and S. R. Shetye (2001): Why is mean sea level along the coast of India higher in the Bay of Bengal than in the Arabian Sea? Geophys. Res. Lett., 28, 563-565.

Shankar, D., P. N. Vinayachandran, and A. S. Unnikrishnan (2002): The monsoon currents in the north Indian Ocean. Progr. Oceanogr., 52, 63-120.

Shenoi, S.S.C., P. K. Saji and A. M. Almeida (1999): Near-surface circulation and kinetic energy in the tropical Indian Ocean derived from Lagrangian drifters. J. Mar. Res., 57, 885-907.

Shetye, S.R., S.S.C. Shenoi, A.D. Gouveia, G.S. Michael, D. Sundar and G. Nampoothiri (1991): Wind-driven coastal upwelling along the western boundary of Bay of Bengal during southwest monsoon. Cont. Shelf Res., 11, 1397-1408.

Shetye, S.R., A.D. Gouveia, S.S.C. Shenoi, D. Sundar, G.S. Michael and G. Nampoothiri (1993): The western boundary current of the seasonal subtropical gyre in the Bay of Bengal, Journal of Geophysical Research, 98, 945-954.

Shetye, S. R., A. D. Gouveia, D. Shankar, S. S. C. Shenoi, P. N. Vinayachandran, D. Sundar, G. S. Michael and G. Nampoothiri (1996): Hydrography and circulation in the western Bay of Bengal during the northeast monsoon. J. Geophys. Res., 101, 14,011-14,025.

Sindhu, B. I. Suresh, A.S. Unnikrishnan, N.V. Bhatkar, S. Neetu and G.S. Michael (2007): Improved bathymetric data sets for the shallow water regions in the Indian Ocean. J. Earth Syst. Sci., 116, 261-274.

SSALTO/DUACS user handbook. 2006. (M)SLA and (M)ADT near-real time and delayed time products. CLS-DOS-NT-06.034, Toulouse, France.

Vignudelli S., P. Cipollini, M. Astraldi, G. P. Gasparini and G. M. R. Manzella (2000): Integrated use of altimeter and in situ data for understanding the water exchanges between the Tyrrhenian and ligurian seas. J. Geophys. Res., 105, 19649-19663.

Vignudelli, S., P. Cipollini, L. Roblou, F. Lyard, G. P. Gasparini, G. Manzella, M. Astraldi (2005): Improved satellite altimetry in coastal systems: Case study of the Corsica Channel (Mediterranean Sea). Geophys. Res. Let., 32, L07608, doi:1029/2005GL22602.

Vinayachandran, P. N., S. R. Shetye, D. Sengupta and S. Gadgil (1996): Forcing mechanisms of the Bay of Bengal circulation. Curr. Sci., 71, 753-763.

Volkov D.L., G. Larnicol and J. Dorandeu (2007): Improving the quality of satellite altimetry data over continental shelves. J. Geophys. Res., 112, doi:10.1029/2006JC003765.

Woodworth, P.L. and R. Player (2003): The Permanent Service for Mean Sea Level: an update to the 21st century. Journal of Coastal Research, 19, 287-295.

Degree	Number of occurrences
0	0
1	45
2	116
3	111
4	0
5	0

Table 1. Number of occurrences of each degree for the polynomial fit of SLA for all the 316 TOPEX/Poseidon cycles during 1992–2001.

Figure captions

Figure 1. Geography of the area, with the positions of 200 m, 1000 m, 2000 m and 3000 m isobaths (bathymetric data taken from Sindhu et al. (2007)). TOPEX/Poseidon coastal altimetric tracks #116 and 155 are shown (thick lines). The diamond represents the location of the Visakhapatnam tide gauge. Altimetric points #9, #23 and #39 of track #116 (used for subsequent analysis) are marked (black crosses).

Figure 2. (a) Long-term standard deviation of the along-track MAP (solid) and along-track AVISO (dashed) SLAs for Topex/Poseidon track #155 at the western boundary of the Bay of Bengal (see Figure 1 for the track location). The standard deviation is plotted as a function of the position of the point along the altimetric track. This position is defined as the distance (in km) from an altimetric point to the shore. (b) Same as (a), but for the number of valid data over the 1992-2002 period. (c) Bathymetry (based on Sindhu et al., 2007) along the altimetric track. Panels (d), (e), and (f) are the same as panels (a), (b), and (c), but are for track #116.

Figure 3. (a) Evolution of the monthly climatology of SLA (in m) for the along-track MAP SLA (dashed line) and for the along-track AVISO SLA (dots), for track #116, point #41 (situated about 47 km offshore) and for the Visakhapatnam tide-gauge SLA (solid). Superimposed in grey (thin solid lines) is the inter-annual envelope of altimetric MAP (tide-gauge) time series. (b) Comparison between the monthly climatology of ship drifts and that of the altimeter-derived currents at 17° N, 84° E. All currents have been projected along the normal to track #116. The thick grey line is the geostrophic current we derived from the MAP data set. The thick black line is the sum of the geostrophic current and the Ekman surface current (computed from ERS scatterometer winds). The dotted line is the geostrophic current derived from along-track AVISO SLA. The ship drifts are from NOAA (dashed line) and Mariano et al. (1995) (dash-dotted line). All currents are positive poleward.

Figure 4. Flow chart of the algorithm. *Ro* is the Rossby radius of deformation.

Figure 5. Sequences of along-track data for track #116 during boreal summer 1994. One frame is shown for each cycle. The horizontal axis is the distance of every altimetric point from the shore (defined as in Figure 2). (a) The crosses represent the raw SLAs (in m) provided by the MAP processing. The cycle number and corresponding date are mentioned in each frame. (b) Same as (a), but for the SLA data cleaned using the 2 m s^{-1} threshold criterion (see section 3). Flagged data (outliers) are shown by grey squares. (c) Same as (a), but superimposed on the polynomial least-squares fit of the cleaned SLA profile (solid curve). The degree of the fitted polynomial is indicated. (d) Geostrophic cross-track surface current (m s^{-1}) derived from (c).

Figure 6. (a) Non-normalized Lomb periodograms of the annual variability of cross-track geostrophic current for TOPEX/Poseidon track #116. The periodogram was computed for the MAP along-track SLAs. The power of the annual component of the cross-track current is plotted as a function of the position of the point along the altimetric track. (b) Same as (a), but for AVISO SLAs, which are extracted along track #116 from the gridded AVISO product. Both (a and b) periodograms exceed the 99% significance level (in the sense described by Press et al. (1992)) throughout the track portion. (c) Long-term standard deviation of the cross-track geostrophic current for the MAP (solid) and AVISO (dashed) SLAs. (d) Bathymetry (based on Sindhu et al. (2007) along the altimetric track.

Figure 7. (a) Non-normalized Lomb periodograms of the cross-track 116 geostrophic current over 1992 to 2001 as a function of the distance to the shore (abscissa) and of the period

(ordinate). One periodogram was computed for each altimetric point, and all the periodograms were then stacked together to produce the 2D plot. Only the values exceeding the 99% significance level are plotted. (b) Same as (a), but extracted at y = 156 days period. (c) Same as (a), extracted at y = 1388 days period. The arrows on (a) show the periods extracted for (b) and (c).

Figure 8. (a) Evolution, during 1993–2000, of the high-passed (intra-seasonal) along-shore MAP altimeter-derived current (m s^{-1}) for point #39 of track #116 (situated 57.7 km offshore, thick grey line), for point #23 (situated 150 km offshore, dotted line) and for point #9 (situated 235 km offshore, black solid line). See text (section 5b) for details of the filter used and Figure 1 for the exact positions of the three points. (b) Same as (a), but for the band-passed (annual) signal. (c) Same as (a), but for the low-passed (inter-annual) signal. (d), (e), (f): Same as (a), (b), (c) respectively, for the AVISO altimeter-derived current.

Figure 9. (a) AVISO SLA (shaded, cm) and surface geostrophic current (vectors, m s^{-1}) for the raw (unfiltered) signal, on 21 May 1994. TOPEX/Poseidon track #116 is shown (white line). Points #9, #23 and #39 are marked (crosses). The shaded area corresponds to the coastal strip, where the fields should be interpreted with caution. (b) Same as (a), but for the annual signal on 15 September 1993. (c) Same as (a), but for the inter-annual signal on 1 June 1999. Note that the grey scale is different for each plot.

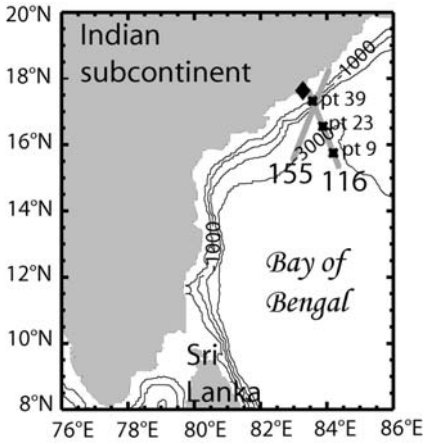

Figure 1.

F. Durand, D. Shankar, F. Birol, S.S.C. Shenoi

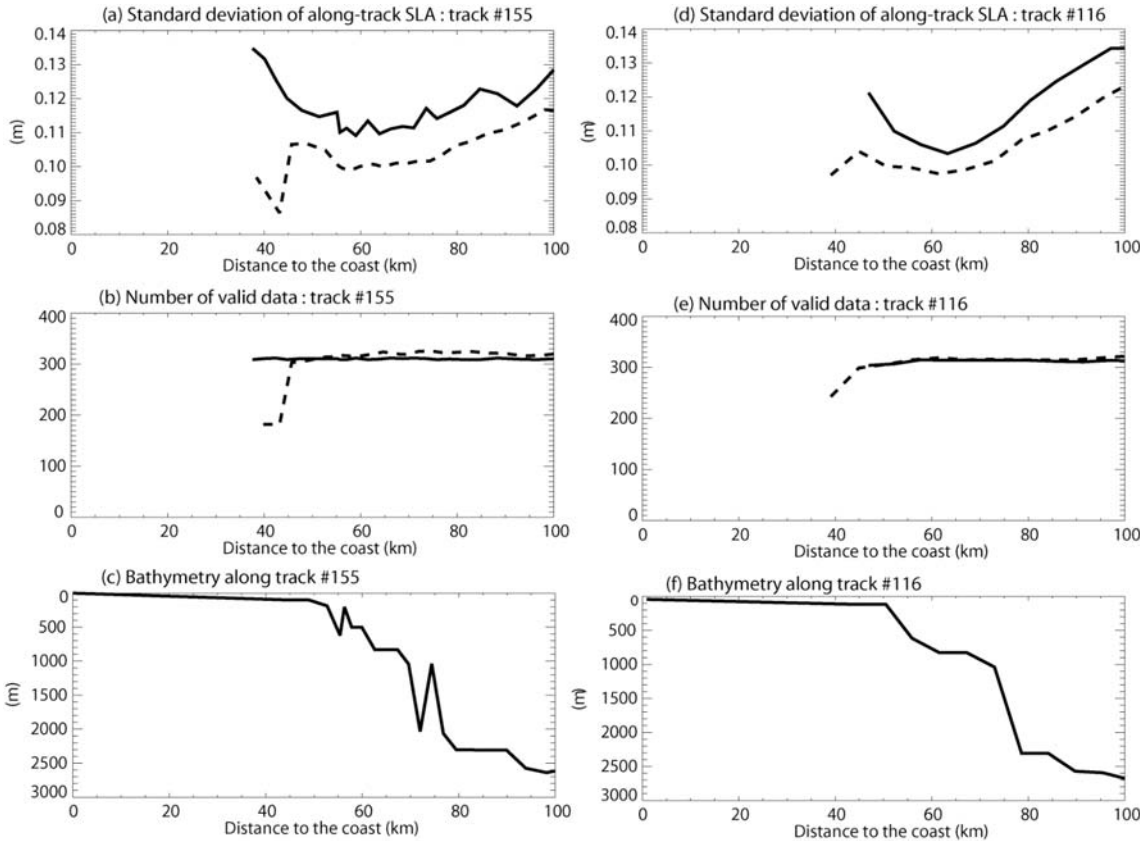

Figure 2.

F. Durand, D. Shankar, F. Birol, S.S.C. Shenoi

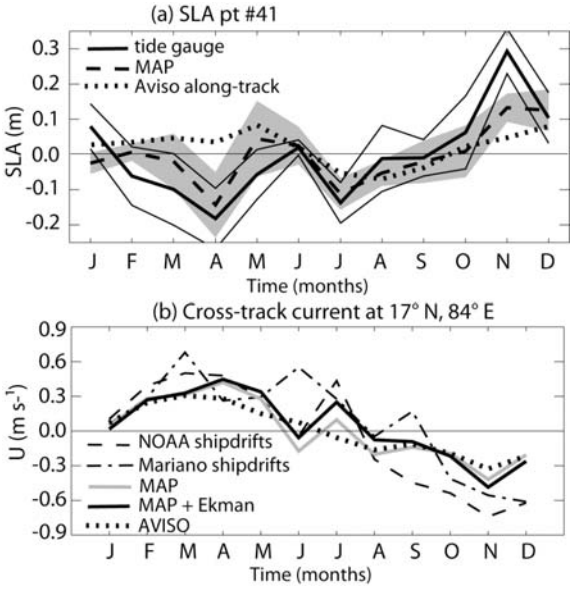

Figure 3.

F. Durand, D. Shankar, F. Birol, S.S.C. Shenoi

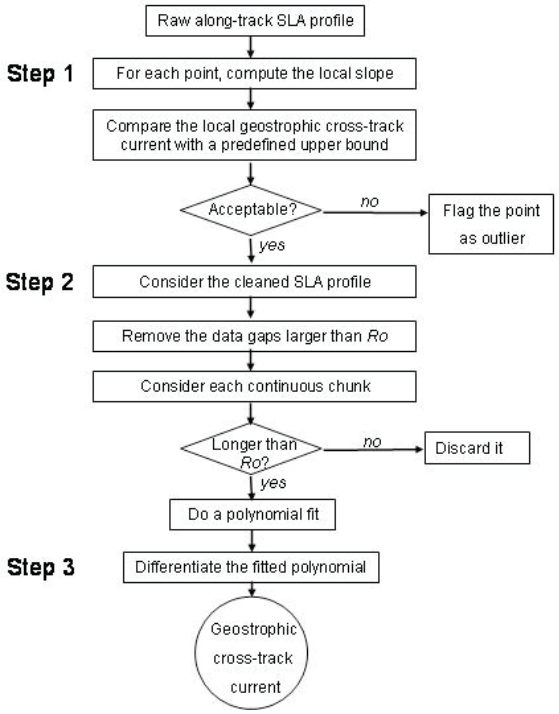

Figure 4.

F. Durand, D. Shankar, F. Birol, S.S.C. Shenoi

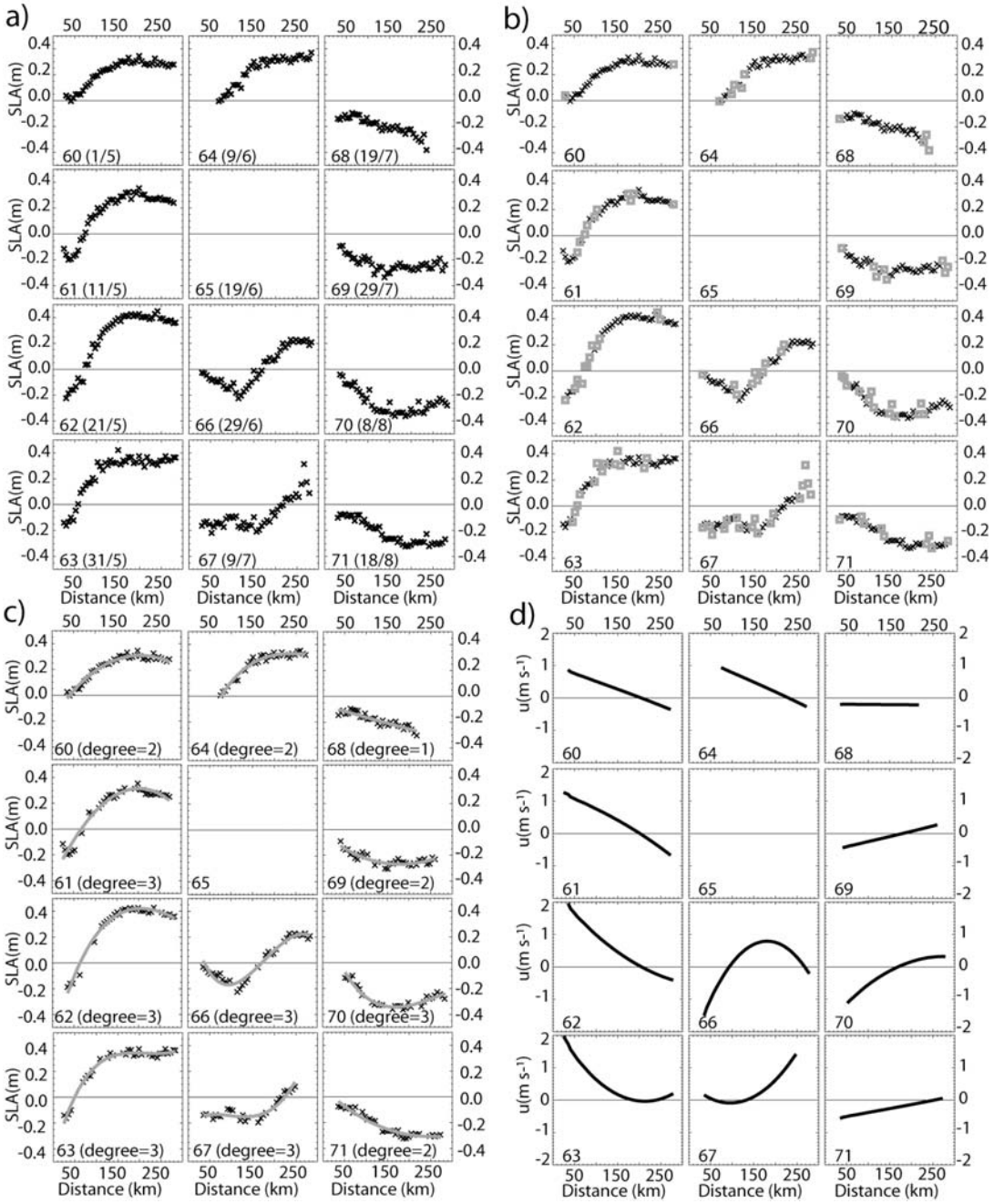

Figure 5.

F. Durand, D. Shankar, F. Birol, S.S.C. Shenoi

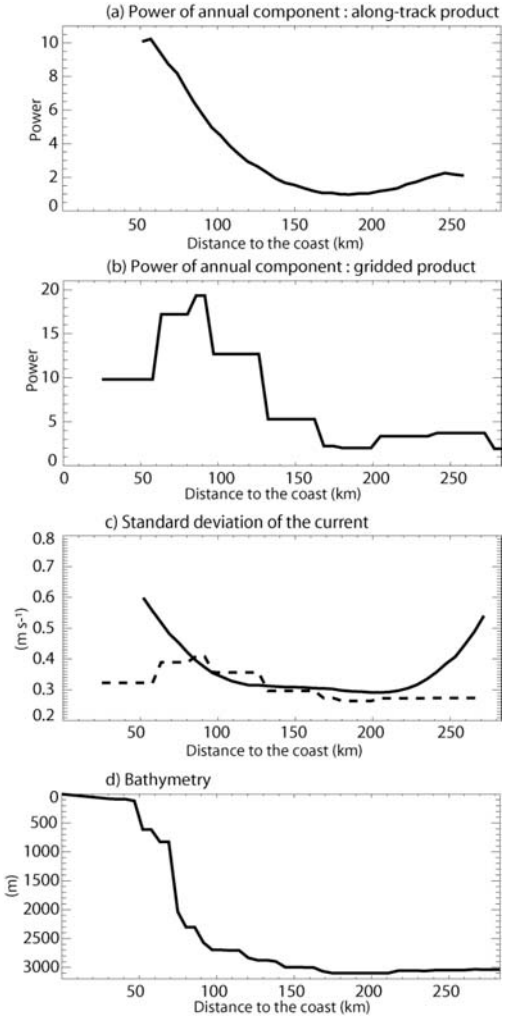

Figure 6.

F. Durand, D. Shankar, F. Birol, S.S.C. Shenoi

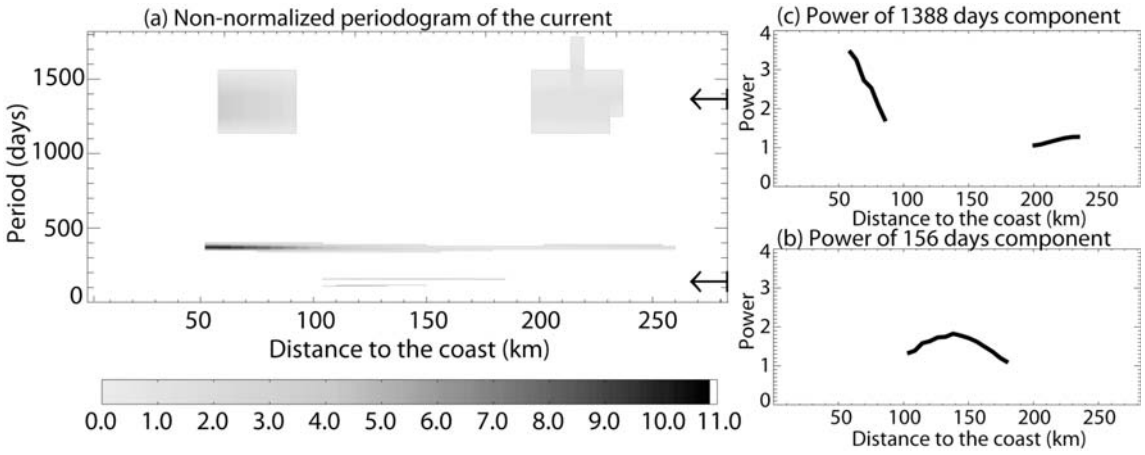

Figure 7.

F. Durand, D. Shankar, F. Birol, S.S.C. Shenoi

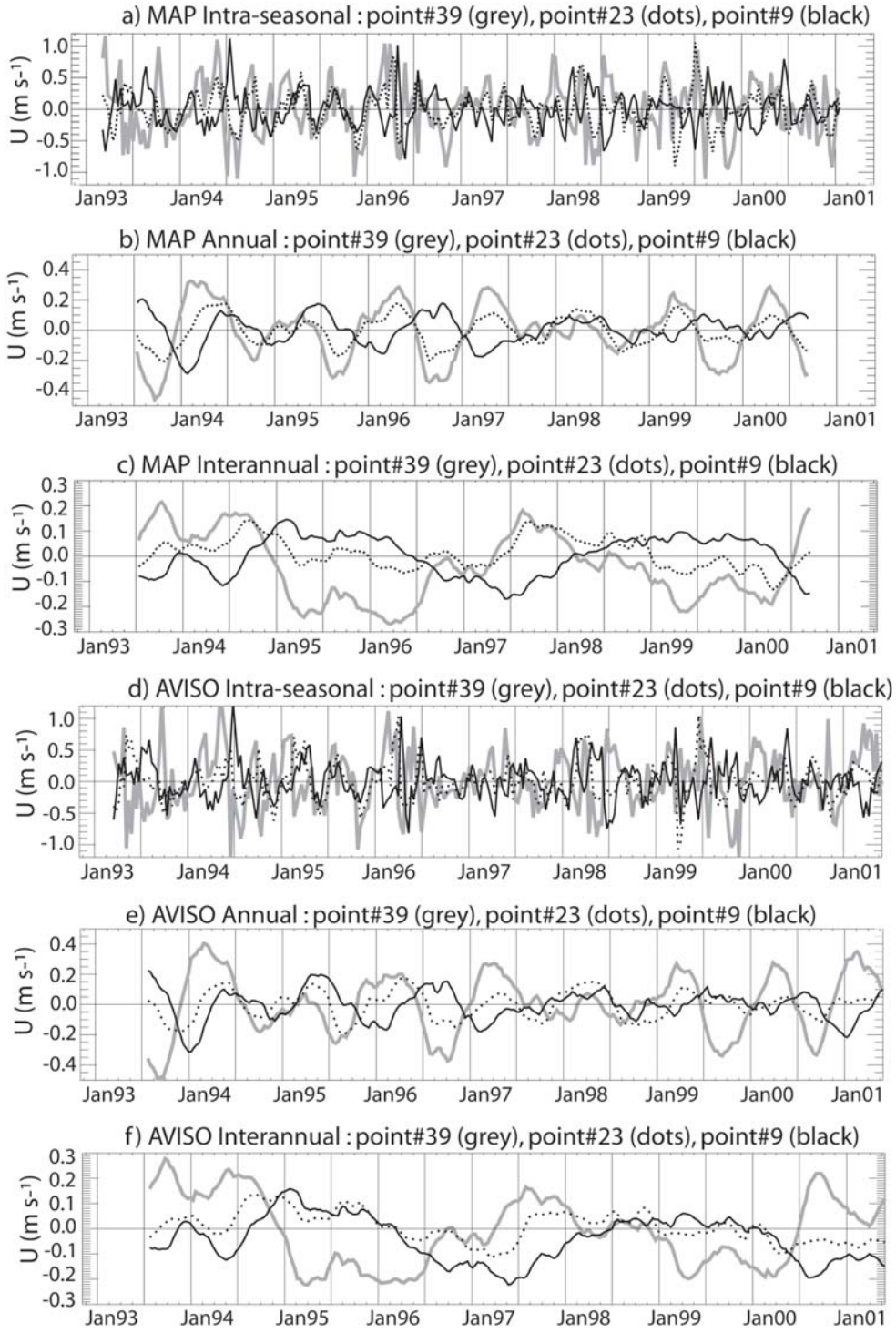

Figure 8.

F. Durand, D. Shankar, F. Birol, S.S.C. Shenoi

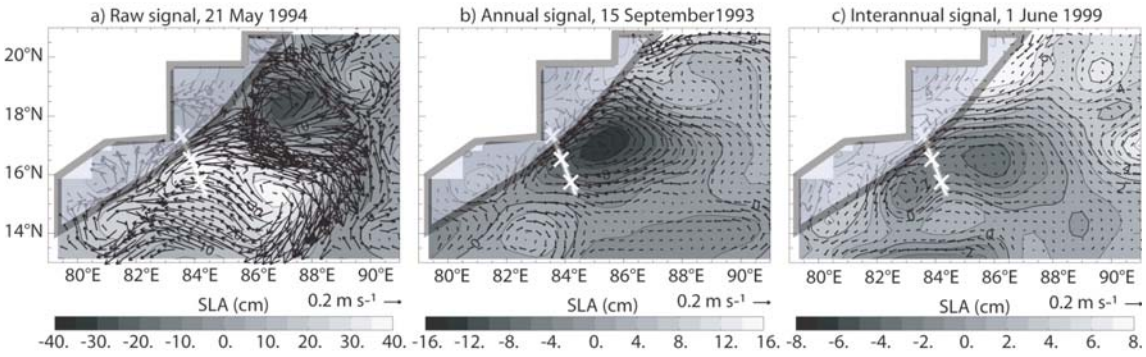

Figure 9.

F. Durand, D. Shankar, F. Birol, S.S.C. Shenoi